Nanoimprint Lithography based Fabrication of Plasmonic Array of Elliptical Nanoholes for Dual Wavelength, Dual Polarisation Refractive Index Sensing

Caoimhe Robinson[1], John Justice[1], Jarno Petäjä[2], Mikko Karppinen[2], Brian Corbett[1], Alan O'Riordan[1] and Pierre Lovera[1,]*

[1] Tyndall National Institute, University College Cork, Cork, Ireland

[2] VTT Technical Research Centre of Finland, Kaitovayla 1. PO Box 1100, FI-90571 Oulu, Finland

[*]pierre.lovera@tyndall.ie

Abstract

We report on the novel fabrication and characterisation of plasmonic arrays of elliptical nanohole, and their use for refractive index based sensing. The substrates were fabricated using nanoimprint lithography into a chromium hard mask followed by transfer of the patterns into the underlying gold layer by dry etching – a combination of processes amendable to mass manufacturing. 3D-FDTD simulations were undertaken and showed the transmission spectrum was dependant upon the polarisation of the incident light, with a series of minima that can be attributed to plasmonic effects on the gold/water or gold/substrate interfaces. Each polarisation showed two peaks on the gold/water interface, one in the visible and one in the near infrared part of the spectrum. Simulated electric field profiles showed that the electric field in the infrared propagates deep in the bulk while the one in the visible was more tightly bound to the surface. Experimental transmission spectra of the fabricated samples showed good agreement with the simulated ones. Bulk refractive index experiments were carried out and sensitivities of 293 nm/RIU and 414 nm/RIU was obtained for the two spectral features of interest when the polarisation was along the long axis of the elliptical nanohole for the visible and infrared features, respectively, and 293 nm/RIU and 323 nm/RIU measured when the polarisation was along the short axis of the nanohole.

Keywords

elliptical, nanoimprint, polarisation, nanohole array, plasmonics

Introduction

Since the discovery of Extraordinary Optical Transmission (EOT) by Ebbessen at al [1], an increasing amount of research has been dedicated to plasmonic nanohole arrays (NHA). In such samples, the momentum mismatch between the light and surface plasmon modes is overcome by the periodic nanostructuring. This leads to maxima and minima at specific wavelength in the transmission spectrum [2]. While more fundamental and experimental work is required to totally understand the EOT phenomenon, it is generally accepted these spectral features reflect the interaction of Localised Surface Plasmon (LSP) of nanohole with Surface Plasmon Polarition (SPP) and Rayleigh anomalies (RA) from the periodic nanostructuring. It is well known that surface plasmons are extremely sensitive to the refractive index at the surface of the metal and this is why they are being increasingly used for label free (bio)sensing [3-5]. The first report of the use of plasmonic NHA for label free sensing was by Brolo et al [6] who detected bovine serum albumin by monitoring the shift of the transmission peak through a gold NHA functionalised with 11-mercaptoundecanoic acid. Since then, significant work has been carried out looking at detecting new chemicals [7-9] or biomaterials [10-21], studying new fluidic delivery approaches [22-26], combining with other sensing techniques such as electrochemistry or Surface Enhanced Raman Scattering [27-32], and integrating into compact handheld devices with new readout approaches [33-37]. The multiplexing capabilities and miniaturisation of NHA are attractive features that have been taken advantage of for a wide variety of applications. However, their lower sensitivities – the limit of detection of plasmonic arrays of circular nanohole have so far not been able to match the one of the classical Kretschmann configuration – have somehow hampered their use for more applications. In order to improve the performance of NHA, approaches based on polarisation dependence have been investigated. Indeed, polarisation modulation can provide enhanced responses either by allowing more accurate interrogation methods or by providing sharper peak features with smaller full width at half maximum. For example, Blanchard-Dionne et al used arrays of circular nanoholes patterned with two periodicities in the –x and –y directions, obtaining two SPP resonances that are spectrally separated. These two resonances were used to provide self-referencing of the laser excitation probe and lead to a fivefold improvement of the signal to noise ratio using this setup compared to a regular transmission measurement [38]. Another way to provide polarisation modulation is to use nanoholes with anisotropic shapes. For example, Lesuffleur et al used double hole arrays and found the the response of their sensor to be comparable to the Kretschmann setup when measuring short-range changes in the refractive index [39]. Similarly, elliptical nanoholes have been shown to have higher transmission with strong polarisation dependence and sharper peaks [40]. These sharper peaks provide superior accuracy when used in a laser based interrogation scheme. Here again, Tellez et al reported performance comparable to Kretschmann-based SPR using arrays of elliptical nanohole [41]. Also, like for the biperiodic arrays, such samples exhibit two spectrally separated resonances – one along the short and one along the long axis of the ellipses. This allows the use of differential detection methods with extremely sharp and intense peaks providing enhanced refractive index sensitivity and associated figure of merit [42].

However, one possible factor currently limiting the uptake of NHA in commercial application is their fabrication cost. Plasmonic arrays of circular nanohole have been fabricated using a variety of techniques including Focused Ion Beam (FIB) milling, e-beam lithography, nanosphere lithography, deep UV lithography, interference lithography, template stripping, and nanoimprint lithography (NIL) [3]. While FIB and e-beam lithography offer tremendous flexibility in terms of hole shape or periodicity of the pattern, these fabrication methods are serial, with high cost and long processing times,

precluding their use for mass manufacturing. Also, while nanosphere and interference lithography techniques allow fabrication at a wafer scale level, it cannot be used for complex nanohole patterns such as crosses or high aspect ratio ellipses that have shown enhanced responsively (vide supra), and the periodicity cannot be adjusted easily. Nanoimprint lithography on the other hand merges the flexibility of e-beam lithography with mass manufacturing scalability and is therefore an attractive method for high throughput fabrication of NHA. Plasmonic arrays of nanodisks and nanohole (circular and square shaped) have been successfully fabricated by nanoimprinting in a resist layer followed by metal evaporation and lift-off [9, 15, 43, 44]. However, while scalable, samples manufactured with such a process flow are prone to rabbit-ear-shaped defects. Also, fabrication of flow through sensors or patterning of nanohole in thicker metal films using this method is challenging.

In this paper, we report on the fabrication of plasmonic arrays of elliptical nanohole using a novel approach based on nanoimprint lithography directly onto a hard mask and subsequent transfer of the patterns in the underlying metal film by anisotropic dry etching. This approach has the potential to overcome the aforementioned limitations of NIL and also allows fabrication of nanostructures in optically active materials that cannot be easily evaporated [45]. In the present work, the geometrical parameters of the NHA (periodicity, shape and dimension of holes) were tailored to give resonances in the near infrared region of the spectrum, where autofluorescence of biological samples is low, and hence reducing biological interferences for biosensor applications. The fabricated nanohole had an elliptical shape so that the array exhibited polarisation dependant transmission spectra, resulting from the coupling of the LSP resonances of the anisotropic shape of the nanohole with the SPP of the periodic pattern. Interestingly, aside from the resonances in the near infrared, the fabricated samples also exhibited, for each polarisation state, a second resonance in the visible part of the spectrum. 3D-FDTD codes were used to simulate the transmission spectra of the sample and good correlation between measurement and simulation were obtained. Bulk refractive index sensing was carried out and dual polarisation, dual wavelength sensing achieved. The 3D-FDTD code was also used to plot the electric field profiles at the wavelengths of interest, and this revealed that the electric field in the infrared propagates deep in the bulk while the one in the visible was more tightly bound to the surface. This difference in the probing depth might be useful for decoupling the contribution from the bulk and the surface in refractive index based label free sensing experiments.

Experimental Section

- *Structure Design and Simulation Methods*

3D-FDTD simulations were undertaken using JFDTD3D [46]. The computational domain for the simulations was chosen to be 630 x 630 x 1600 nm^3, with a mesh of 5 nm in all directions. Periodic boundary conditions (630 nm) in the x and y directions were employed to simulate an infinite square array. Permittivity of gold was modelled using Drude plus two-pole Lorentz model. The dielectric constants used for the glass substrate was $\varepsilon_{glass} = 2.25\varepsilon_0$ and was $\varepsilon_{water} = 1.77\varepsilon_0$ for the water superstrate. Perfectly Matching Layers boundary conditions were imposed in the z direction in order to avoid reflections from the edges of the computational window. Transmission spectra were deconvoluted by Fourier transforming the simulated electric and magnetic fields on the surface above the gold followed by construction of the surface integral of the outward Poynting vector.

- *Fabrication*

The arrays of elliptical nanohole in thin gold film were fabricated using nanoimprint lithography and dry etching, see schematics 1.

- Wafer before patterning:

(Ti 5 nm/Au 50 nm) layers were blanket deposited by evaporation (Temescal FC-2000 E-beam evaporator) on top of a silicon wafer with 200 nm of silicon dioxide. The gold was then covered by a 50 nm Cr layer that was subsequently used as a hard mask.

- Nanoimprint lithography

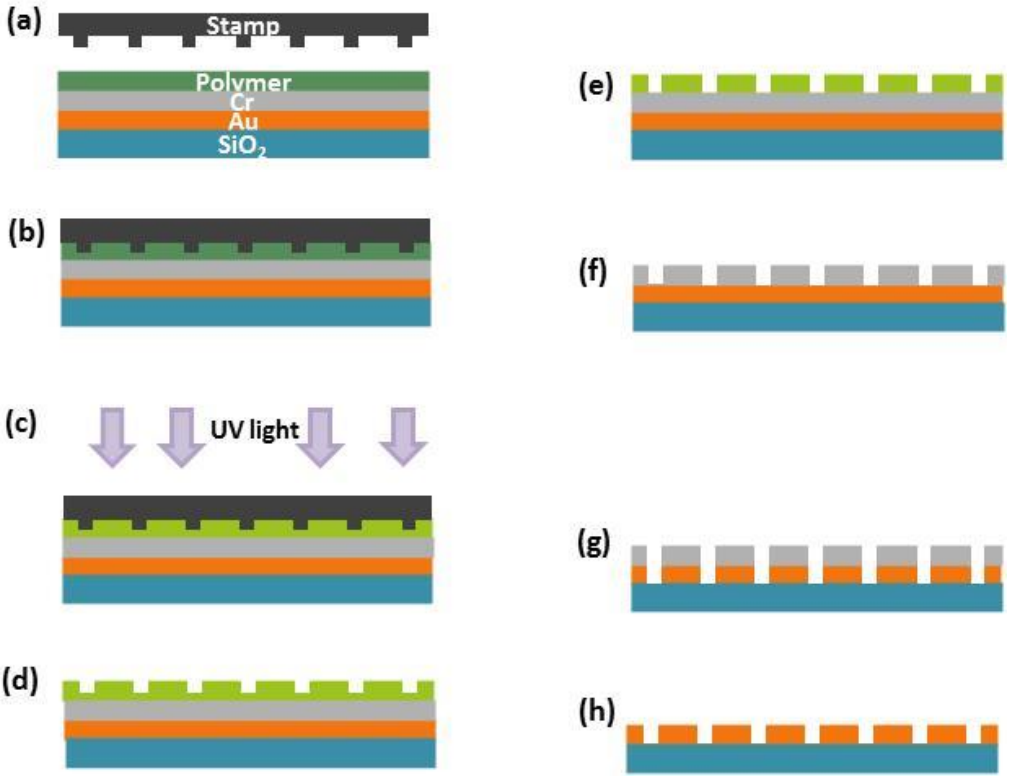

Schematic 1 Resist patterning with working stamp into UV-sensitive polymer followed by dry etching features into the Au substrate.

This UV-based nanoimprint lithography process is represented in Scheme 1 (a-e). Nanoimprints were made by Obducat's Eitre 6 Nano Imprint Lithography (NIL) tool. For NIL fabrication of the nanohole structures the first quartz master stamp carrying the elliptical nanohole structures was fabricated by e-beam lithography (University of Eastern Finland) and subsequently used to produce the nanoimprint working stamp, which consisted of the complementary features (i.e. nanopillars). The working stamp was made by Eitre 6 by taking a replica of the master to the OrmoStamp material (Micro Resist Technology GmbH). A borosilicate wafer (diam. 4", thickness 0,7mm, Finnish SpecialGlass) was used as a substrate for the thin (~10µm) OrmoStamp layer.

To start the actual NIL process, a UV-sensitive polymer (mr-UVCur-21, Micro Resist Technology GmbH) was spin coated onto the substrate to allow for transfer of the nanofeatures (Scheme 1a). The working stamp, which is UV transparent, was pressed into the polymer in vacuum in order to avoid entrapped

air (Scheme 1b). The stack was then nanoimprinted in the Eitre 6 where UV light cured the polymer (Scheme 1c), leaving behind the nanohole structures once the stamp is detached (Scheme 1d). The residual polymer layer was removed by anisotropic plasma etching (Scheme 1e).

- Dry etching

The features that have been nanoimprinted in the resist are then transferred into the Cr layer using a dry etch. Chromium was used as a hard mask as the selectivity of the Au etch against the nanoimprint resist was poor, only allowing shallow features to be etched. With the additional chromium layer, further etching was possible allowing full transfer of the nanoholes into the gold. The parameters for transferring the features from the nanoimprinted resist into the chromium hard mask can be found in table 1.

Table 1 Parameters for the Cr etch

Cr dry etch	
Parameters	**Value**
Cl_2 gas flow	26 sccm
O_2 gas flow	4 sccm
H_2 gas flow	10 sccm
Coil power	400 W
Platen power	20 W
Chamber pressure	10 mT
Temperature	100°C

Table 2 Parameters for the Au etch

Au dry etch	
Parameters	**Value**
CF4 flow	12 sccm
CHF3 flow	28 sccm
Coil power	800 W
Platen power	75 W
Chamber pressure	2.5 mT
Temperature	10°C

The features were then transferred from the chrome hard mask to the gold layer using the etch from table 2. Once the etching was complete, the Cr hard mask was removed using Lodyne Chrome etchant, resulting in a thin Au layer with nanohole arrays.

- *Optical Measurements*

Experimental spectra in the visible region were acquired using a MicroTime 200 (PicoQuant) setup with a 50x lens (LMPlanFLN, 0.5 N.A, Olympus). The slit width was set at 50 µm and a 300 grooves grating was used. Maximum light intensity was utilised with a 2 s integration time. A 2” x 2” Dichroic Film Polarizer (Thorlabs) was placed in the path of the excitation light. For the near-IR spectra, a 600 µm internal diameter optical fibre was connected to a Leica optical microscope and an Ando

spectrum analyser was employed to record the spectrum. Maximum light intensity was again used, with a LPVis100-MP Polarizer from Thorlabs to polarize the excitation light. For both systems, water was injected into a transparent microfluidic cell which allowed for the plasmonic array to be immersed. The collected spectra were normalised to polarised light transmitted through an unpatterned area of the Au film.

- *SEM Characterisation*

The nanohole arrays were viewed using a Jeol Scanning electron Microscope. An emission current of 5 µA and acceleration voltage of 2-5 kV were used.

Results and Discussion

- Predicted spectral location of SPP

The chosen design of 100 µm square arrays with 350 nm x 150 nm diameter holes orientated at 45^0 was similar to that used in previous work [47], but with the periodicity customised to obtain a refractive index sensitive Surface Plasmon Polaritons (SPP) into the desired infrared spectral region. This periodicity was calculated using equation 1, which predicts the spectral positions of the SPP on the glass/Au and Au/water interfaces of the arrays (this equation is intrinsic as ε_{Au} is dependant on λ)

$$\lambda_{SPP} = \frac{P}{(i^2+j^2)^{1/2}} \left(\frac{\varepsilon_{Au}\varepsilon_d}{\varepsilon_{Au}+\varepsilon_d}\right) \qquad (1)$$

The position of Rayleigh anomalies (RA) can also be calculated using equation 2. [48]

$$\lambda_{RA} = \frac{P}{(i^2+j^2)^{1/2}} \sqrt{\varepsilon_d} \qquad (2)$$

Where P is the periodicity of the design, i and j are integers which define the order of the Bloch mode, ε_{Au} is the permittivity of the gold and ε_d is the permittivity of the adjacent dielectric material.

Table 3 Solutions to equations (1) and (2) predicting the spectral position of Surface Plasmon Polariton and Rayleigh Anomaly on the glass/Au and Au/air interfaces.

Surface Plasmon Polariton (SPP)		**Rayleigh Anomaly (RA)**	
Order	**Wavelength (nm)**	**Order**	**Wavelength (nm)**
$(1,0)_{Au\text{-}Glass}$	971	$(1,0)_{Au\text{-}Glass}$	945
$(1,0)_{Au\text{-}Water}$	862	$(1,0)_{Au\text{-}Water}$	837
$(1,1)_{Au\text{-}Glass}$	714	$(1,1)_{Au\text{-}Glass}$	668
$(1,1)_{Au\text{-}Water}$	641	$(1,1)_{Au\text{-}Water}$	592

As seen in table 3, there is an expected refractive index sensitive SPP on the Au-water interface in both the visible and near-infrared region. These equations predict spectral locations, but do not inform on the transmission specifics of a hole or account for the effects of polarisation on the anisotropic elliptical nanohole arrays.

- 3D-FDTD Simulations

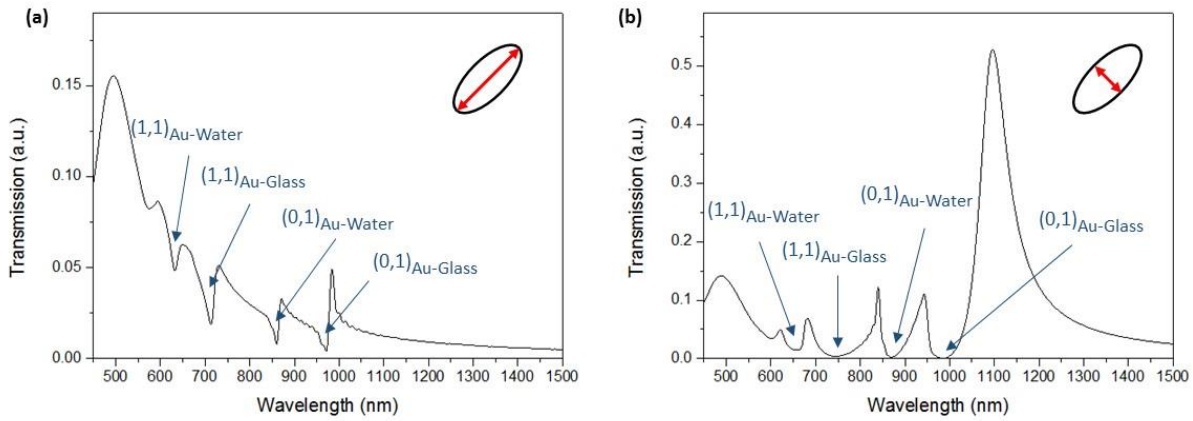

Figure 1 3D-FDTD Simulated transmission spectra of arrays of elliptical nanohole in water with incident light polarised along the (a) long axis and (b) the short axis of the nanohole.

To gain more insight about the polarisation dependence of the transmission spectra, 3D-FDTD simulations were carried out (using water as superstrate) with incident light polarised along the short and along the long axis of the ellipses, see Figure 1. Both spectra exhibited several minima in transmission associated with SPP and RA. When the incident light was polarized along the long axis of an ellipse, Figure 1 (a), a series of very sharp spectral minima at λ=972 nm, λ=861 nm, λ=714nm and λ=631 could be observed. These minima in the transmission spectrum can be correlated to the $(1, 0)_{Au\text{-}Glass}$, $(1, 0)_{Au\text{-}Water}$, $(1, 1)_{Au\text{-}Glass}$ and $(1, 1)_{Au\text{-}Water}$ SPP/RA modes on the metal/dielectric interface from Table 3, respectively. When the incident light was polarized along the short axis of the ellipses, the transmission reached zero for λ=980 nm, λ=875 nm, λ=745 nm and λ=646 nm, Figure 1 (b). As for the other polarisation, these minima can be associated with the aforementioned $(1, 0)_{Au\text{-}Glass}$, $(1, 0)_{Au\text{-}Water}$, $(1, 1)_{Au\text{-}Glass}$ and $(1, 1)_{Au\text{-}Water}$ SPP/RA. Both spectra also show a broad peak around λ = 490 nm, with a transmission of ~15%, which corresponds to direct transmission (intraband transition) for gold and occurs irrespective of the incident polarization [49].

In order to confirm the nature of the spectral features, and the interface they occur on, the electric field distributions for polarisation along the ellipse's long axis were plotted for the different wavelengths of interest, see Figure 2.

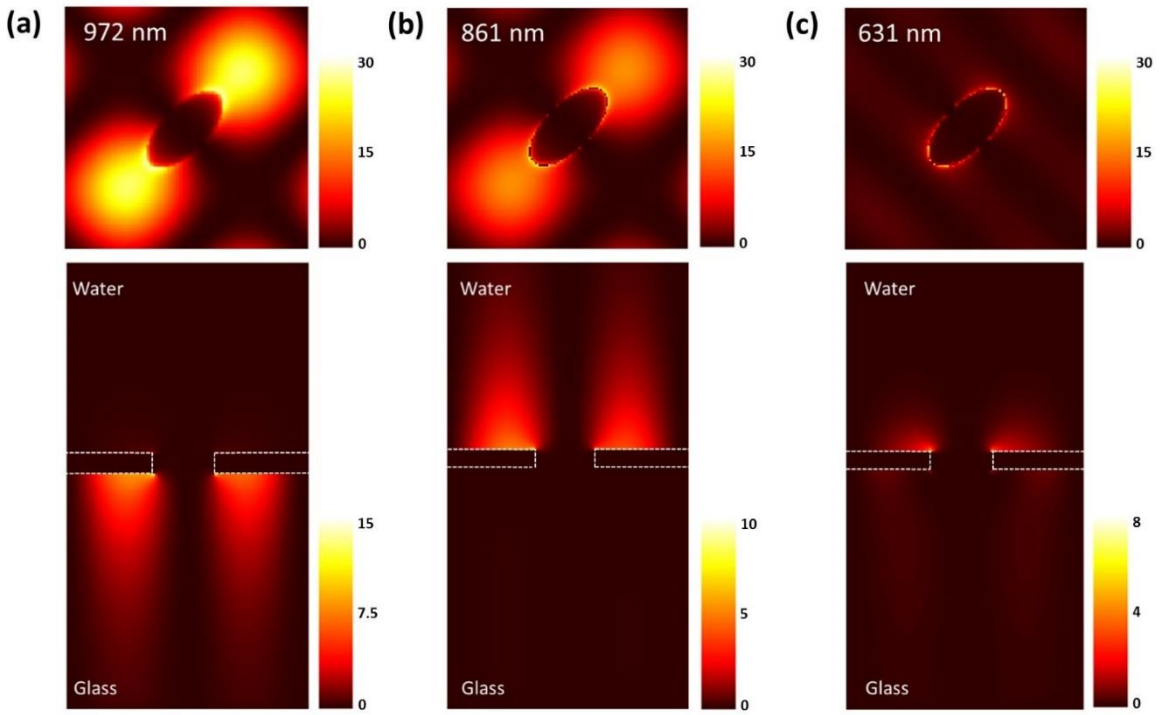

Figure 2 FDTD calculated frequency-resolved $|Ez|^2$ profiles at (a) λ = 972nm, (b) λ = 861nm and (c) λ = 631 nm with incident light polarized along the long axis of the ellipses. Top panels show near field profiles 10 nm below (a) and above (b and c) the Au film and bottom shows cross sections across the middle of the ellipses.

Figure 2(a) shows the electric field profile on the glass side at the minimum in transmission at 972nm. In the top panel, it can be seen that the field profile possesses a hybrid character, being both localized to the rim of the ellipse and propagating along the interface in the (1, −1) direction. This mode thus results from the combination of the LSP of the nanohole and the $(1, 0)_{Au\text{-}Glass}$ SPP/RA at 972nm. The side view shows the electric field is escaping from the surface, which is a signature of a Rayleigh anomaly [50]. A similar response is seen at 861nm, see Figure 2 (b), except this time the electric field profile is escaping on the superstrate side. This corresponds to the $(1,0)_{Au\text{-}Water}$ SPP/RA, which will be sensitive to changes in surrounding dielectric medium. Finally, the side elevation view seen in Figure 2 (c) shows the electric field distribution due to $(1,1)_{Au\text{-}Water}$ SPP/RA at 631 nm. It shows light escaping from the substrates on the superstrate – albeit not as much as in the case of the $(1,0)_{Au\text{-}Water}$ SPP/RA. Interestingly, the profile also shows the light escaping on the substrate side, marking the onset of the $(1,1)_{Au\text{-}Glass}$ SPP/RA. As can be seen in figure 2 (b) and (c), the two resonances on the water interface are different profile, with the resonance in the infrared propagating deeper in the bulk while the one in the visible is more tightly bound. These two resonances have therefore two probing depth and this can be used to decouple refractive index changes contributed by the bulk from surface-binding events following the methods described by Hossain et al [51].

Similarly, with the light polarised along the short axis of the ellipse (not shown), there are two refractive index sensitive dips, $(1,1)_{Au\text{-}Water}$ at 646 nm and the $(1,0)_{Au\text{-}Water}$ at 861 nm.

- SEM Characterisation of the fabricated samples

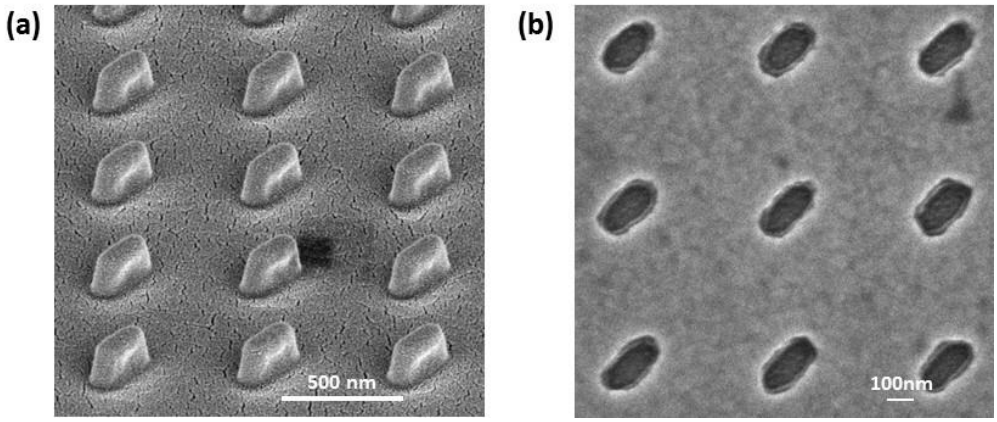

Figure 3 SEM image of (a) the OrmoStamp and (b) the fabricated elliptical nanohole array.

Figure 3 shows a SEM image of the OrmoStamp used for the NIL process together with the fabricated elliptical nanohole array. The nanohole features in the fabricated devices were 110 ± 11 nm x 222 ± 18 nm and the periodicity 630 nm, see Figure 3 (b). The dimensions of the nanohole were a bit smaller than the ones targeted initially and simulated (150 nm x 350 nm). These discrepancies in the dimensions of the designed and fabricated nanoholes may be due to the OrmoStamp not sufficiently imprinting into the UV-sensitive polymer. After the samples were made the depth of the nanoholes in quartz master were inspected by making a cross section cut with focused ion beam (FIB) milling and taking SEM pictures. These measurements revealed uneven etch depth in the different locations of the wafer. The target depth was 200 nm and measured values varied between 205 and 280 nm. This means that the spinned polymer layer was thinner than the pillar height. Indeed, Figure 3 (a) shows that the inverted nanopillar features of the OrmoStamp have sloping walls, resulting in a smaller area at the pillar tip that at the pillar base. This affects also to the final size of the nanoholes. Sloping walls origin from the quartz master. Sloping walls are beneficial in imprinting since it makes the detaching of the working stamp easier after imprint. The smaller dimensions of the nanohole however did not preclude plasmonics effects to occur and transmission spectra were taken in water and spectral features were seen in the expected regions.

- Experimental Transmission Spectra

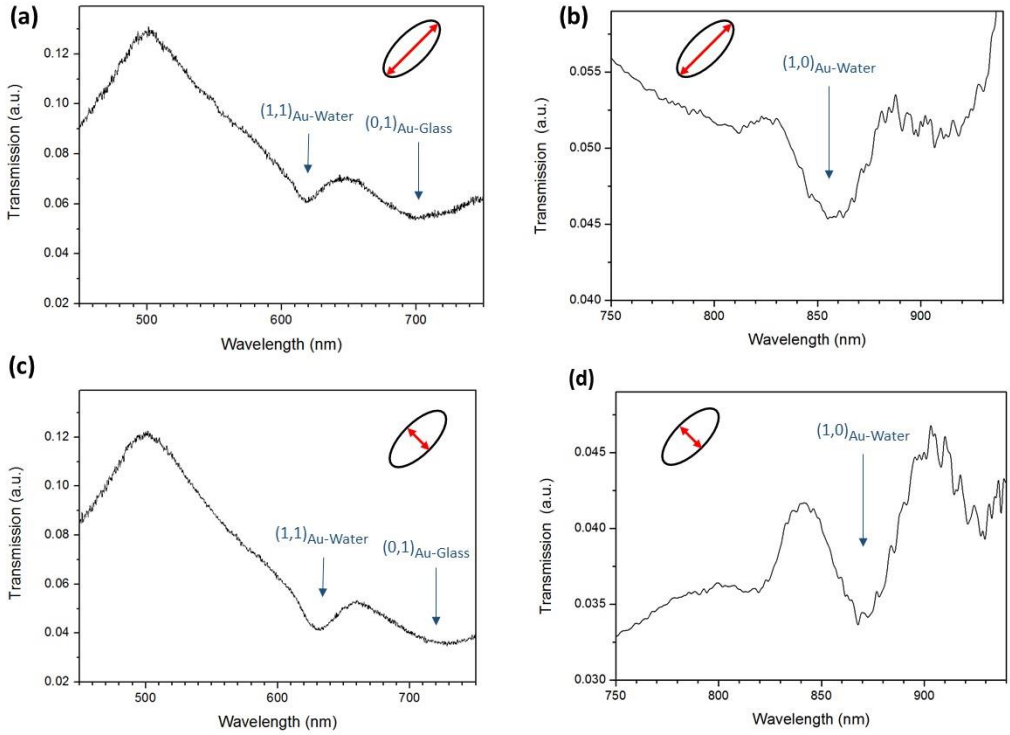

Figure 4 Experimental transmission spectra through the nanohole array with incident light polarised along the long axis in the visible region (a) and the near-IR region (b), and with incident light polarised along the short axis in the visible region (c) and the near-IR region (d).

Figure 4 shows the transmission spectra with the incident light polarised along the long (a and b) and short (c and d) axis of the ellipses. For the spectra taken in water with the polarisation along the long axis of the ellipse, the $(1,1)_{Au\text{-}Water}$ SPP/RA minimum is found at 619nm, approx. 12 nm lower than predicted by the simulation. However, there is strong conformity with the $(1,0)_{Au\text{-}Water}$ SPP/RA feature lying at 858nm (861 nm simulated), as seen in Fig 4(b). Similarly, the $(1,1)_{Au\text{-}Water}$ SPP/RA and $(1,0)_{Au\text{-}Water}$ SPP/RA spectral minima when the incident light is polarised along the short axis can be found at 631 nm (646nm simulated) and 871nm (861 nm simulated), respectively, see Figure 4(c). These dissimilarities in the actual and expected spectra can be attributed to the smaller size of the fabricated nanohole as compared to the simulated ones. Regardless of these irregularities, there is an overall good correlation between the measured and simulated spectra, with two spectral features present in the visible and NIR region for each polarisation.

- Refractive Index Sensing in Bulk Solution

To demonstrate the substrate's ability to track changing refractive indices in bulk solutions, transmission spectra were taken with the arrays submerged in deionised water and iso-propyl alcohol (IPA), see Figure 5.

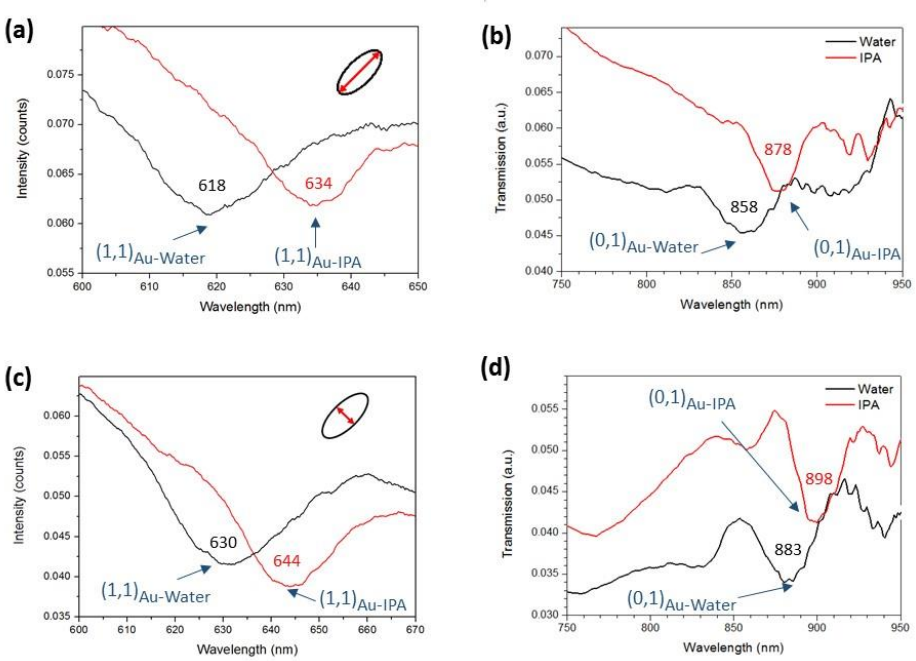

Figure 5 Transmission spectra in water and IPA with incident light polarised along the long axis in the visible region (a) and the near-IR region (b). Transmission spectra in water and IPA with incident light polarised along the short axis in the visible region (c) and the near-IR region (d).

As expected, the spectral features occurring on the superstrate side exhibit a shift as the refractive index increases from 1.33 (water) to 1.38 (IPA). Interestingly, the shift can be observed for the two peaks and for the two polarisations. The spectral sensitivity, S, shows the relationship between the change in wavelength with the change in refractive index ($S = \Delta\lambda/\Delta n$) and is a typical Figure of Merit used for arrays of nanohole. With light polarised along the long axis of the ellipse, the spectral sensitivity of the (1,1) SPP/RA was 336 nm/RIU and 414 nm/RIU for the (1,0) SPP/RA. With our experimental setup, this translates to resolutions of $2.9 * 10^{-4}$ RIU and $2.4 * 10^{-4}$ RIU, respectively. The spectral sensitivity with light polarised along the short axis of the ellipse was measured to be 293 nm/RIU for the (1,1) SPP/RA and 323 nm/RIU for the (1,0) SPP/RA, or resolutions of $3.4 * 10^{-4}$ RIU and $3.1 * 10^{-4}$ RIU, respectively. These values are typical for NHA, with sensitivities between 271 nm/RIU and 630 nm/RIU reported in the visible and near infrared range [2]. In the present work, being able to monitor the shifts of two spectrally separated peaks probing different depths might allow the discrimination of the bulk contribution from the true surface contribution in refractive index based label free sensing. Also, the ability to do this for two polarisation states provides internal validation and reduces the chances of getting false positive results.

Conclusion

Substrates containing plasmonic arrays of elliptical nanoholes were successfully fabricated using a novel approach combining nanoimprint lithography into a hard mask followed by transfer of the patterns into the underlying gold layer by dry etching. This fabrication process is compatible with mass manufacturing and has therefore the potential to overcome current limitations preventing the uptake of NHA in commercial applications. 3D-FDTD simulation was carried out and revealed the transmission spectrum was dependant on the polarisation of the incident light, with two minima attributed to plasmon effects on the gold water interface observed in the visible and near infrared. The 3D-FDTD code was also used to plot of the electric field profiles at the wavelengths of interest, and this revealed that the electric field in the infrared propagates deep in the bulk while the one in the visible was more tightly bound to the surface. Good overall correlation was obtained between the simulated and experimental transmission spectra. Bulk refractive index experiments were carried out on the fabricated sample and sensitivities of 293 nm/RIU and 414 nm/RIU obtained for the two peaks when the polarisation was along the long axis of the elliptical nanohole and 293 nm/RIU and 323 nm/RIU measured when the polarisation was along the short axis of the nanohole.

Acknowledgments

This work was supported by the EU-funded project Phast-ID (FP7-ICT-2009-5-258238) and the EPA project UisceSense (2015-W-MS-21).

References

1. Ebbesen, T.W., et al., *Extraordinary optical transmission through sub-wavelength hole arrays.* Nature, 1998. **391**: p. 667.
2. Blanchard-Dionne, A.-P. and M. Meunier, *Sensing with periodic nanohole arrays.* Advances in Optics and Photonics, 2017. **9**(4): p. 891-940.
3. Escobedo, C., *On-chip nanohole array based sensing: a review.* Lab on a Chip, 2013. **13**(13): p. 2445-2463.
4. Lovera, P., et al., *Low-cost silver capped polystyrene nanotube arrays as super-hydrophobic substrates for SERS applications.* Nanotechnology, 2014. **25**(17): p. 175502.
5. Wong, C.L. and M. Olivo, *Surface Plasmon Resonance Imaging Sensors: A Review.* Plasmonics, 2014. **9**(4): p. 809-824.
6. Brolo, A.G., et al., *Surface Plasmon Sensor Based on the Enhanced Light Transmission through Arrays of Nanoholes in Gold Films.* Langmuir, 2004. **20**(12): p. 4813-4815.
7. Wright, J.B., et al., *Chemoselective gas sensors based on plasmonic nanohole arrays.* Optical Materials Express, 2012. **2**(11): p. 1655-1662.
8. Lindquist, N.C., M.A. Turner, and B.P. Heppner, *Template fabricated plasmonic nanoholes on analyte-sensitive substrates for real-time vapor sensing.* Rsc Advances, 2014. **4**(29): p. 15115-15121.
9. Le, A.P., et al., *Functional Nanoimprinted Plasmonic Crystals for Chemical Sensing and Imaging*. Nanoplasmonic Sensors, ed. A. Dmitriev. 2012. 199-227.
10. Chuo, Y., et al., *Large-Area Low-Cost Flexible Plastic Nanohole Arrays for Integrated Bio-Chemical Sensing.* Ieee Sensors Journal, 2013. **13**(10): p. 3982-3990.
11. Barrios, C.A., et al., *Aluminum Nanohole Arrays Fabricated on Polycarbonate for Compact Disc-Based Label-Free Optical Biosensing.* Plasmonics, 2014. **9**(3): p. 645-649.
12. Bottazzi, B., et al., *Multiplexed label-free optical biosensor for medical diagnostics.* Journal of Biomedical Optics, 2014. **19**(1).

13. Im, H., et al., *Label-free detection and molecular profiling of exosomes with a nano-plasmonic sensor.* Nature Biotechnology, 2014. **32**(5): p. 490-U219.
14. Cetin, A.E., et al., *Plasmonic Nanohole Arrays on a Robust Hybrid Substrate for Highly Sensitive Label-Free Biosensing.* Acs Photonics, 2015. **2**(8): p. 1167-1174.
15. Ding, T., et al., *Quantification of a Cardiac Biomarker in Human Serum Using Extraordinary Optical Transmission (EOT).* Plos One, 2015. **10**(3).
16. Li, X., et al., *Plasmonic nanohole array biosensor for label-free and real-time analysis of live cell secretion.* Lab on a Chip, 2017. **17**(13): p. 2208-2217.
17. Cetin, A.E., et al., *Plasmonic Sensor Could Enable Label-Free DNA Sequencing.* Acs Sensors, 2018. **3**(3): p. 561-568.
18. Soler, M., et al., *Multiplexed nanoplasmonic biosensor for one-step simultaneous detection of Chlamydia trachomatis and Neisseria gonorrhoeae in urine.* Biosensors & Bioelectronics, 2017. **94**: p. 560-567.
19. Yanik, A.A., et al., *Seeing protein monolayers with naked eye through plasmonic Fano resonances.* Proceedings of the National Academy of Sciences of the United States of America, 2011. **108**(29): p. 11784-11789.
20. Gordon, R., et al., *A New Generation of Sensors Based on Extraordinary Optical Transmission.* Accounts of Chemical Research, 2008. **41**(8): p. 1049-1057.
21. Yanik, A.A., et al., *An Optofluidic Nanoplasmonic Biosensor for Direct Detection of Live Viruses from Biological Media.* Nano Letters, 2010. **10**(12): p. 4962-4969.
22. Niu, L.F., et al., *Integrating plasmonic diagnostics and microfluidics.* Biomicrofluidics, 2015. **9**(5).
23. Monteiro, J.P., et al., *Microfluidic Plasmonic Biosensor for Breast Cancer Antigen Detection.* Plasmonics, 2016. **11**(1): p. 45-51.
24. Escobedo, C., et al., *Flow-Through vs Flow-Over: Analysis of Transport and Binding in Nanohole Array Plasmonic Biosensors.* Analytical Chemistry, 2010. **82**(24): p. 10015-10020.
25. Zehtabi-Oskuie, A., J.G. Bergeron, and R. Gordon, *Flow-dependent double-nanohole optical trapping of 20 nm polystyrene nanospheres.* Scientific Reports, 2012. **2**: p. 966.
26. Yoshikawa, T., et al., *Optical Trap-Mediated High-Sensitivity Nanohole Array Biosensors with Random Nanospikes.* The Journal of Physical Chemistry Letters, 2017. **8**(2): p. 370-374.
27. Atighilorestani, M., et al., *Electrochemical Control of Light Transmission through Nanohole Electrode Arrays.* ACS Photonics, 2016. **3**(12): p. 2375-2382.
28. Galvan, D.D., et al., *Surface-Enhanced Raman Scattering on Gold Nanohole Arrays in Symmetrical Dielectric Environments Exhibiting Electric Field Extension.* The Journal of Physical Chemistry C, 2016. **120**(44): p. 25519-25529.
29. Zheng, P., et al., *Tailoring plasmonic properties of gold nanohole arrays for surface-enhanced Raman scattering.* Physical Chemistry Chemical Physics, 2015. **17**(33): p. 21211-21219.
30. Lee, S.H., et al., *Self-Assembled Plasmonic Nanohole Arrays.* Langmuir, 2009. **25**(23): p. 13685-13693.
31. Brolo, A.G., et al., *Nanohole-Enhanced Raman Scattering.* Nano Letters, 2004. **4**(10): p. 2015-2018.
32. Skehan, C., et al., *Plasmonic and SERS performances of compound nanohole arrays fabricated by shadow sphere lithography.* Nanotechnology, 2018. **29**(9).
33. Yesilkoy, F., et al., *Phase-sensitive plasmonic biosensor using a portable and large field-of-view interferometric microarray imager.* Light-Science & Applications, 2018. **7**.
34. Coskun, A.F., et al., *Lensfree optofluidic plasmonic sensor for real-time and label-free monitoring of molecular binding events over a wide field-of-view.* Scientific Reports, 2014. **4**.
35. Cetin, A.E., et al., *Handheld high-throughput plasmonic biosensor using computational on-chip imaging.* Light-Science & Applications, 2014. **3**.
36. Guyot, L., et al., *Integrated silicon-based nanoplasmonic sensor.* Optics Express, 2011. **19**(10): p. 9962-9967.

37. Seiler, S.T., I.S. Rich, and N.C. Lindquist, *Direct spectral imaging of plasmonic nanohole arrays for real-time sensing.* Nanotechnology, 2016. **27**(18).
38. Blanchard-Dionne, A.P., et al., *Intensity based surface plasmon resonance sensor using a nanohole rectangular array.* Optics Express, 2011. **19**(16): p. 15041-15046.
39. Lesuffleur, A., et al., *Periodic nanohole arrays with shape-enhanced plasmon resonance as real-time biosensors.* Applied Physics Letters, 2007. **90**(24): p. 243110.
40. Gordon, R., et al., *Strong polarization in the optical transmission through elliptical nanohole arrays.* Physical Review Letters, 2004. **92**(3).
41. Tellez, G.A.C., et al., *Atomically flat symmetric elliptical nanohole arrays in a gold film for ultrasensitive refractive index sensing.* Lab on a Chip, 2013. **13**(13): p. 2541-2546.
42. Ai, B., et al., *Plasmonic sensor with high figure of merit based on differential polarization spectra of elliptical nanohole array.* Nanoscale, 2017. **9**(38): p. 14710-14721.
43. Nishiguchi, K., et al., *Fabrication of gold-deposited plasmonic crystal based on nanoimprint lithography for label-free biosensing application.* Japanese Journal of Applied Physics, 2016. **55**(8).
44. Mona, J.K.K., et al., *Inexpensive and fast wafer-scale fabrication of nanohole arrays in thin gold films for plasmonics.* Nanotechnology, 2010. **21**(20): p. 205301.
45. Md Nazmul, H., et al., *High aspect ratio nano-fabrication of photonic crystal structures on glass wafers using chrome as hard mask.* Nanotechnology, 2014. **25**(35): p. 355301.
46. JDFTD3D, *www.thecomputationalphysicist.com.*
47. Lovera, P., et al., *Polarization tunable transmission through plasmonic arrays of elliptical nanopores.* Optics Express, 2012. **20**(23): p. 25325-25332.
48. Ghaemi, H.F., et al., *Surface plasmons enhance optical transmission through subwavelength holes.* Physical Review B, 1998. **58**(11): p. 6779-6782.
49. Gao, H., J. Henzie, and T.W. Odom, *Direct Evidence for Surface Plasmon-Mediated Enhanced Light Transmission through Metallic Nanohole Arrays.* Nano Letters, 2006. **6**(9): p. 2104-2108.
50. Chang, S.-H., S.K. Gray, and G.C. Schatz, *Surface plasmon generation and light transmission by isolated nanoholes and arrays of nanoholes in thin metal films.* Optics Express, 2005. **13**(8): p. 3150-3165.
51. Hossain, M.N., et al., *Dual resonance approach to decoupling surface and bulk attributes in photonic crystal biosensor.* Optics Letters, 2014. **39**(21): p. 6213-6216.